university of groningen

University Medical Center Groningen

University of Groningen

Ordered mesoporous SiO_2 nanoparticles as charge storage sites for enhanced triboelectric nanogenerators

Li, Wenjian; Xiang, Yinyu; Zhang, Wei; Loos, Katja; Pei, Yutao

Published in:
Nano energy

DOI:
10.1016/j.nanoen.2023.108539

IMPORTANT NOTE: You are advised to consult the publisher's version (publisher's PDF) if you wish to cite from it. Please check the document version below.

Document Version
Publisher's PDF, also known as Version of record

Publication date:
2023

Link to publication in University of Groningen/UMCG research database

Citation for published version (APA):
Li, W., Xiang, Y., Zhang, W., Loos, K., & Pei, Y. (2023). Ordered mesoporous SiO_2 nanoparticles as charge storage sites for enhanced triboelectric nanogenerators. *Nano energy*, *113*, Article 108539. https://doi.org/10.1016/j.nanoen.2023.108539

Copyright
Other than for strictly personal use, it is not permitted to download or to forward/distribute the text or part of it without the consent of the author(s) and/or copyright holder(s), unless the work is under an open content license (like Creative Commons).

The publication may also be distributed here under the terms of Article 25fa of the Dutch Copyright Act, indicated by the "Taverne" license. More information can be found on the University of Groningen website: https://www.rug.nl/library/open-access/self-archiving-pure/taverne-amendment.

Take-down policy
If you believe that this document breaches copyright please contact us providing details, and we will remove access to the work immediately and investigate your claim.

Downloaded from the University of Groningen/UMCG research database (Pure): http://www.rug.nl/research/portal. For technical reasons the number of authors shown on this cover page is limited to 10 maximum.

Nano Energy 113 (2023) 108539

Contents lists available at ScienceDirect

Nano Energy

journal homepage: www.elsevier.com/locate/nanoen

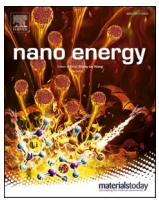

Full paper

Ordered mesoporous SiO_2 nanoparticles as charge storage sites for enhanced triboelectric nanogenerators

Wenjian Li [a], Yinyu Xiang [a], Wei Zhang [a], Katja Loos [b], Yutao Pei [a,*]

[a] Department of Advanced Production Engineering, Engineering and Technology Institute Groningen, Faculty of Science and Engineering, University of Groningen, Nijenborgh 4, 9747 AG Groningen, the Netherlands

[b] Macromolecular Chemistry & New Polymeric Materials, Zernike Institute for Advanced Materials, Faculty of Science and Engineering, University of Groningen, Nijenbogh 4, 9747AG, Groningen, the Netherlands

ARTICLE INFO

Keywords:
Mesoporous SiO_2
Nanoparticles
Charge storage
TENG

ABSTRACT

Triboelectric nanogenerators (TENGs) have demonstrated great prospects in energy harvesting and self-powered sensing. However, the surface triboelectric charges are very easy to dissipate in the air atmosphere, especially after the contact electrification stops. Here, we propose ordered mesoporous SiO_2 (OMS) nanoparticles with a large specific surface area (SSA) as effective body charge storage sites inside polydimethylsiloxane (OMS-PDMS) to enhance the output performance of TENGs. With the addition of 1 wt% OMS nanoparticles, the transferred charges of the TENG showed a sharp enhancement, rising from 21 nC to 60 nC. The enhancement effect of OMS nanoparticles on the output increased linearly with SSA. In addition, the OMS-PDMS also demonstrated a superior charge retention ability, with 68 % of the voltage being retained over a long time after the contact separation motion stopped, while that of the pure PDMS quickly dropped to near zero. The instantaneous output power density of the TENG with OMS-PDMS reached 5.26 W/m^2, which is a 25-fold enhancement. This work proposed OMS nanoparticles with a large SSA as effective charge storage sites to enhance the output performance of TENGs.

1. Introduction

There are many types of ambient energy, including wind, vibration, raindrops, water waves and even body motion, which are typically random, low-frequency and microscale and are usually wasted due to the lack of effective technologies for harvesting these types of energy. Fortunately, the invention of the triboelectric nanogenerator (TENG) has enabled the efficient utilization of these energies by converting them into electricity based on the working principle of contact electrification and electrostatic induction [1–3]. By virtue of the advantages of various working modes, high efficiency, high output, universal material choice and easy fabrication, TENGs have demonstrated giant prospects not only in energy harvesting as power sources [4–7] for electronics and sensor nodes but also in self-powered sensing [8–14] as active sensing components for wearables and industrial monitoring. Whether for energy harvesting and self-powered sensing, the output performance of the TENG must always be as high as possible for practical applications. The output performance of the TENG is mainly dependent on the surface charge density of the triboelectric material [15], which relies on the intrinsic contact electrification performance between the triboelectric materials. For two certain materials, the maximum number of charges that can be transferred to each other in the atmosphere is limited [16]. To further improve the surface charge density, many strategies have been proposed, such as surface micropatterning [17], chemical modification [18], and charge injection [19]. Charge injection, specifically, is considered to be one of the most efficient ways to largely improve the surface charge density. However, surface charges tend to quickly dissipate, especially in high humidity and high temperature environments; therefore, the enhanced surface charge density will gradually decline, and the output of the TNEG will accordingly decrease.

Compared to surface charges, body charges inside triboelectric materials have a much slower dissipation speed and can stay for quite a long time [20,21]. Under a high electric field and large charge concentration gradient, a portion of surface charges can penetrate into the interior of triboelectric materials due to charge drift and diffusion [22]. However, if there are no effective charge traps or storage sites inside the material, the penetrated body charges will eventually either recombine with opposite charges induced on the electrodes or dissipate into the

* Corresponding author.
E-mail address: y.pei@rug.nl (Y. Pei).

https://doi.org/10.1016/j.nanoen.2023.108539
Received 29 March 2023; Received in revised form 10 May 2023; Accepted 16 May 2023
Available online 18 May 2023
2211-2855/© 2023 The Author(s). Published by Elsevier Ltd. This is an open access article under the CC BY license (http://creativecommons.org/licenses/by/4.0/).

atmosphere. Incorporating nanomaterials that have strong electron capture or storage ability into triboelectric materials has been proven to be an effective approach to retain body charges and finally improve the total charge density [20]. The amount of charges that can be trapped or stored inside the material depends not only on the inherent electron attracting ability but also on the specific surface area (SSA) of the nanomaterials. Therefore, some nanomaterials featuring a high specific surface area, such as 2D materials [22–26] and porous materials [27–29], are particularly popularly applied as fillers in polymer matrices to maximize the amount of stored charges. Very recently, Baik and co-workers achieved the highest transferred charge density of TENGs fabricated with various triboelectric materials by adding a SiO_2 nanoparticle layer between the MoS_2 triboelectric layer and Ni electrode [30]. The transferred charge density increased from 338.7 to 1072 $\mu C/m^2$, and the charge retention ability was also enhanced from 60 % to 81 %. In addition, SiO_2 is also a well-known electret material that has been widely applied in microelectromechanical system (MEMS) energy harvesting devices due to its high charge storage and retention ability

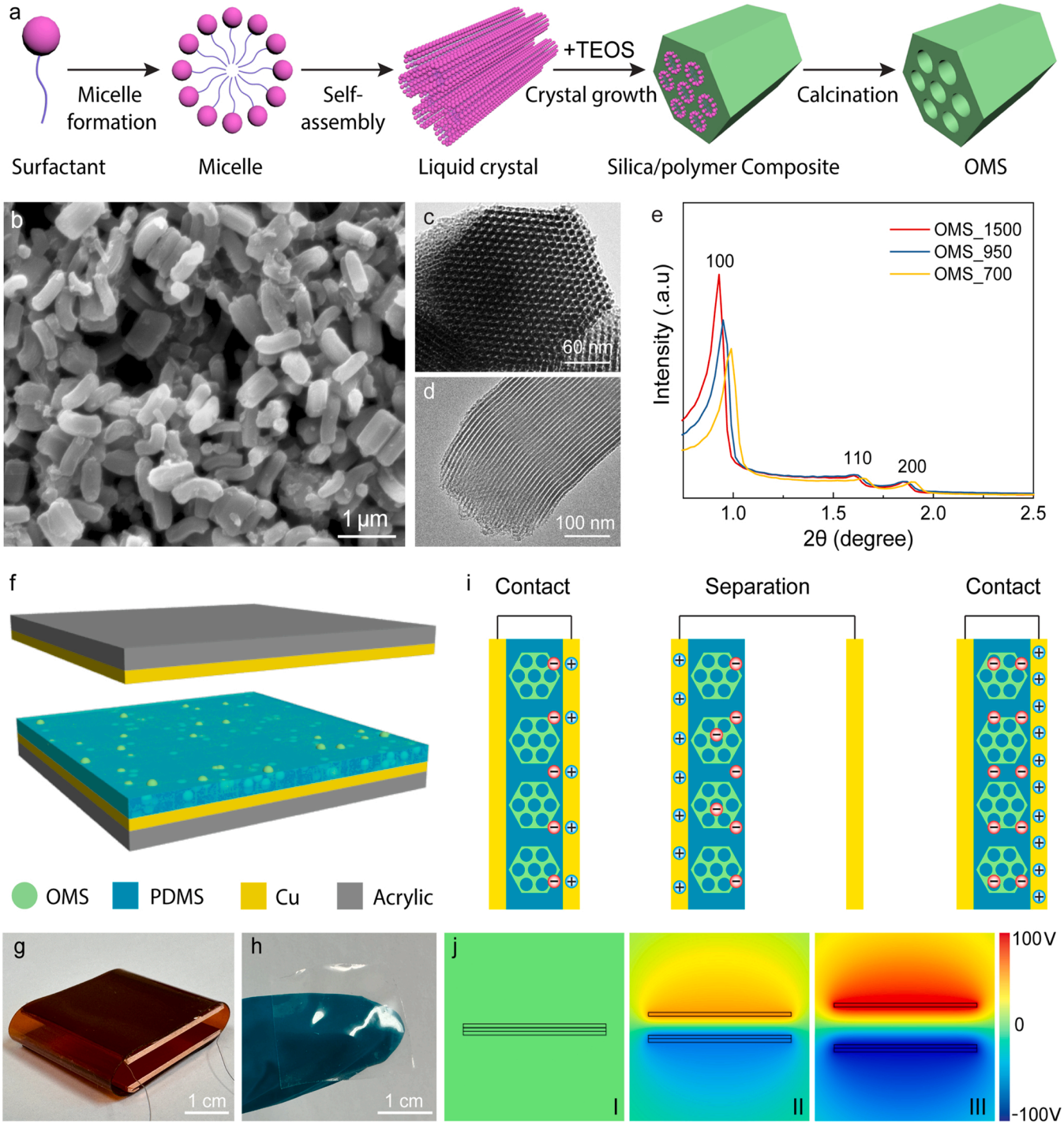

Fig. 1. (a) Synthesis procedure of OMS nanoparticles. (b) SEM image of OMS_700 nanoparticles. TEM image of (c) cross-section view and (d) lateral view of OMS_700 nanoparticles. (e) XRD pattern of the OMS nanoparticles with different sizes. (f) Schematic structure and (g) photo of the TENG composed of the OMS-nanoparticle/PDMS composite. (h) Photo of the transparent OMS-PDMS triboelectric layer. (i) Working principle of the TENG with OMS nanoparticles acting as body charge trappers. (j) Electrical potential distribution simulation of the TENG at contacted, separating, and separated states.

[31–33].

Herein, we propose ordered mesoporous SiO_2 (OMS) nanoparticles with a large specific surface area as effective body charge storage sites inside polydimethylsiloxane (OMS-PDMS) to enhance the output performance of TENGs. When the concentration of OMS nanoparticles increased to 1 wt%, the transferred charges of the TENG sharply increased from 21 nC to 60 nC due to the enhancement from the extra body charges stored by OMS nanoparticles. With higher concentrations, the enhancement effect began to decrease due to the reduced effective contact electrification area of PDMS since OMS nanoparticles appeared on the surface of the composite. Three different sizes of OMS nanoparticles with varying SSAs were synthesized, and their influence on the output performance of the TENG was investigated. All three kinds of OMS nanoparticles contributed an obvious enhancement to the output, and it was found that the enhancement effect increased linearly with the SSA of the OMS nanoparticles. Compared to pure PDMS, OMS-PDMS also demonstrated an enhanced charge retention ability. After the cease of contact electrification, the open-circuit voltage of the TENG with OMS-PDMS can retain 68 %, while that of the pure PDMS quickly dropped to near 0 V. The instantaneous output power density of the TENG with OMS-PDMS reached 5.26 W/m^2, which is 25 times higher than that of pure PDMS. This work proposed OMS nanoparticles with a large specific surface area as effective charge storage sites to enhance the output performance of TENGs.

2. Results and discussion

Fig. 1a shows the synthesis procedure of the OMS nanoparticles, which involves P123 micelle formation, self-assembly between micelles and TEOS, crystal growth, and finally the removal of the P123 surfactant (calcination). During the synthesis procedure, P123 served as the soft template, glycerol was the cosolvent, TEOS was the silicon feedstock, and HCl provided the acid environment. The as-synthesized OMS nanoparticles were first characterized with scanning electron microscopy (SEM) and transmission electron microscopy (TEM). Uniform rod-like nanoparticles were observed in the SEM image (Fig. 1b), which also demonstrates that the OMS nanoparticles have an average length of 700 nm. Consequently, the OMS nanoparticles were coded according to their average length, such as OMS_700, OMS_950 and OMS_1500, where the numbers represent the average length of OMS nanoparticles in nm. The TEM image in Fig. 1c shows the transverse cross-section of the OMS nanoparticle, clearly revealing a hexagon outline. In addition, it can be seen that regular parallel pore channels run along the long axis of the OMS nanoparticles from the TEM image of side view (Fig. 1d), which confirms the typical two-dimensional hexagonal mesoporous structures (P6mm) [34]. The small angle X-ray diffraction (XRD) patterns of OMS nanoparticles all exhibit a sharp peak at 2-theta of approximately 1° and two weaker peaks between 1.5° and 2°, corresponding to (100), (110), and (200) diffractions associated with p6mm hexagonal symmetry (Fig. 1e) [35].

The high-SSA OMS nanoparticles were blended into PDMS to fabricate a high-performance TENG. The structure of the TENG is schematically illustrated in Fig. 1f, which works in the contact-separation mode. A layer of OMS-PDMS was spin-coated on a Cu electrode-coated acrylic substrate and served as the negative triboelectric layer. The positive triboelectric layer is another Cu layer that simultaneously acts as another electrode, which is also deposited on an acrylic substrate. Fig. 1g and 1h show the photo of the assembled TENG (5 × 5 cm^2) and of the transparent OMS-PDMS triboelectric layer (thickness: ~100 μm), respectively. A photo of the structure of the TENG before assemblage is shown in Fig. S1 (of the supporting information). The working principle of the TENG is based on contact electrification and electrostatic induction, as illustrated in Fig. 1i. When the Cu layer and OMS-PDMS layer contact each other, electrons begin to transfer from the surface of the Cu layer to the surface of OMS-PDMS due to their difference in electron affinity. The separation of the two charged surfaces can result in a potential difference between the two electrodes, which consequently drives electron flow from the left Cu electrode to the right Cu electrode. Similarly, electrons will flow back from the right electrode to the left electrode when the Cu layer and OMS-PDMS layer are in contact again. It is worth noting that during reciprocating contact-separation, surface electrons can penetrate into the interior of the PDMS due to electron drift caused by the high electric field and electron diffusion resulting from the electron concentration gradient. These electrons can be captured and stored by the OMS nanoparticles until reaching the saturation state. Then, the TENG works in a stable state with saturated charge transfer in each cycle. The electric potential distributions of the TENG in fully contacted (I), separating or contacting (II) and fully separated (III) states are simulated, as demonstrated in Fig. 1j.

The influence of the OMS concentration on the output performance of the TENG was first studied. The surface morphologies of the OMS-PDMS with different concentrations (0, 0.6, 1, 1.5 and 2 wt%) of OMS_950 nanoparticles were investigated through 3D surface profilometry and are shown in Fig. 2a. The pure PDMS showed a smooth surface morphology, while those mixed with OMS_950 nanoparticles featured apparent rough surfaces. Fig. 2b summarizes the measured average surface roughness (Ra) of the OMS-PDMS with varying concentrations of OMS nanoparticles. The pure PDMS had a very low Ra of 1.88 nm. With the increase in the concentration of OMS_950 nanoparticles, the Ra of the OMS-PDMS first increased and reached a maximum (33.07 nm) at an OMS concentration of 1.5 wt% and then decreased when the OMS concentration further increased to 2 wt%. The decrease in the roughness at high OMS concentrations is likely due to the aggregation of OMS nanoparticles. Fig. 2c and 2d show SEM images of the surface of the pure PDMS and 1 wt% OMS-PDMS, respectively, which reveal that the rough surface of OMS-PDMS is because some OMS nanoparticles appear at the surface of the PDMS. SEM images of the surfaces of OMS-PDMS with different concentrations are also demonstrated in Fig. S2.

The open-circuit voltage (V_{OC}), short-circuit current (I_{SC}) and short-circuit transferred charge (Q_{SC}) of the TENG tested under a working load of 20 N and a frequency of 0.5 Hz with different OMS_950 concentrations are shown in Fig. 2**e-g**, respectively. With pure PDMS, the V_{OC}, I_{SC} and Q_{SC} of the TENG were 51 V, 3.5 μA and 21 nC, respectively. After adding OMS nanoparticles, the output of the TENG first obviously increased due to the charge storage ability of the OMS nanoparticles. The best output performance was reached at a 1 wt% concentration of OMS nanoparticles with V_{OC}, I_{SC} and Q_{SC} values of 156 V, 10.5 μA and 55.4 nC, respectively. When the OMS concentration further increased to over 1 wt%, the output of the TENG showed a decreasing trend. At an OMS concentration of 1.5 wt%, the output of the TENG slightly decreased, and the V_{OC}, I_{SC} and Q_{SC} were 125 V, 7.8 μA and 38 nC, respectively. As the OMS concentration continued to increase to 2 wt%, the V_{OC}, I_{SC} and Q_{SC} of the TENG further dropped to 99 V, 6.2 μA and 29 nC, respectively. To determine the reason behind the output change over OMS concentrations, the hydrophobicity of OMS-PDMS with different OMS_950 concentrations was first investigated since SiO_2 has a hydrophilic property, which may affect the surface hydrophobicity of OMS-PDMS and decrease the output performance when the OMS concentration is sufficiently high. As shown in Fig. S3, all OMS-PDMS demonstrated similar water contact angles (WCAs), so the hydrophilic property of OMS nanoparticles could be excluded from the possible causes for the output decrease at higher OMS concentrations. Then the dielectric constant of the OMS-PDMS films was measured and the result is shown in Fig. S4, from which one can see that the dielectric properties of OMS-PDMS did not show obvious change after adding OMS nanoparticles. The surface potential of the pure PDMS and OMS-PDMS with 1 wt% OMS nanoparticles before and after contact were also measured with kelvin probe force microscopy (KPFM). As shown in Figs. 2**h** and 2**i**, the OMS-PDMS had a similar surface potential (−0.42 V) to that of the pure PDMS (−0.41 V) before contact because no charge is stored in OMS before contact. After contact, the surface potential of pure PDMS

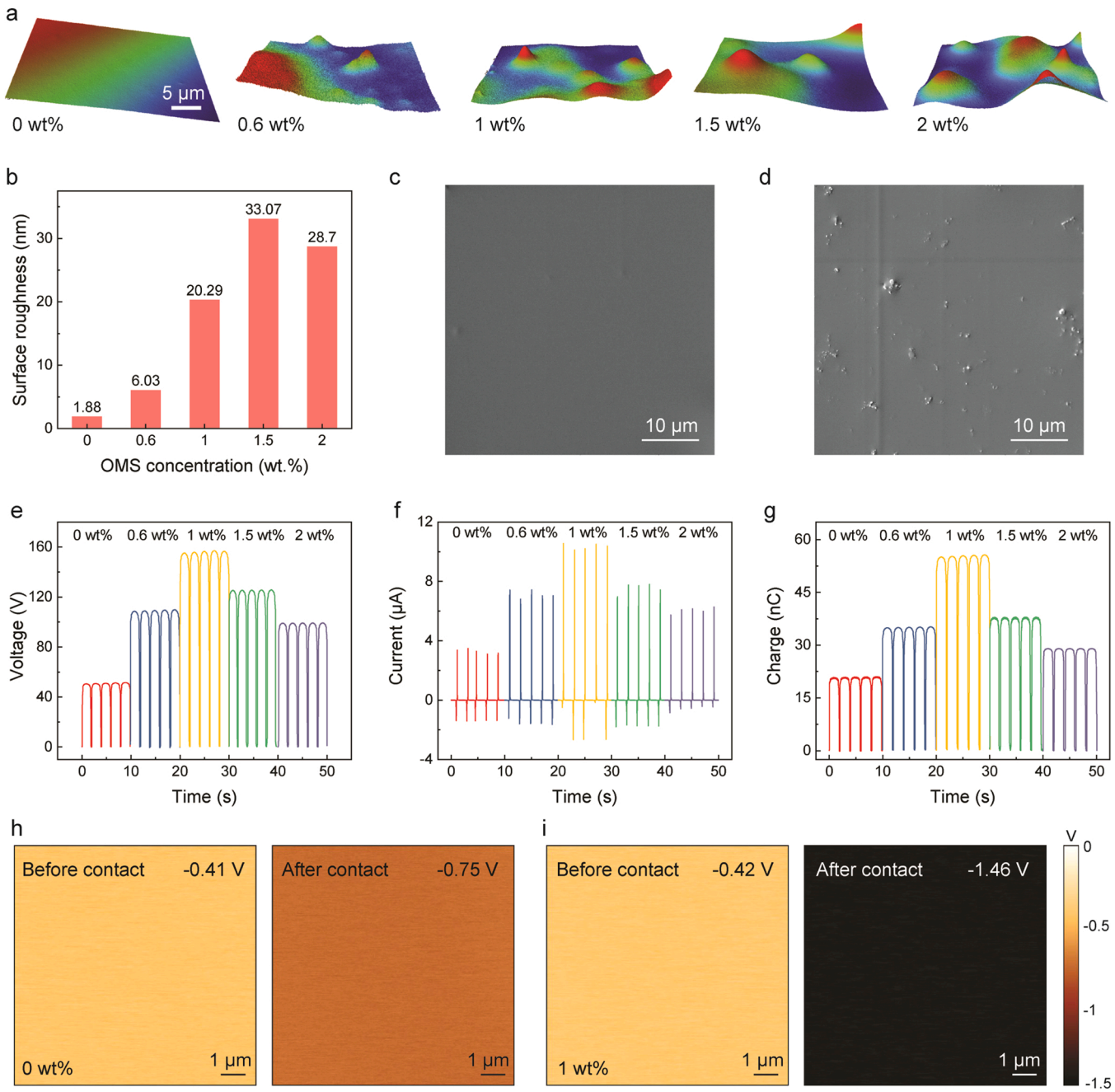

Fig. 2. (a) Surface morphology of OMS-PDMS with different concentrations of OMS nanoparticles. (b) Average surface roughness of the OMS-PDMS with different OMS concentrations. SEM image of (c) pure PDMS and (d) OMS-PDMS with 1 wt% OMS_950. (e) V_{OC}, (f) I_{SC} and (g) Q_{SC} of the TENG with different concentrations of OMS nanoparticles. KPFM surface potential measurements of (h) pure PDMS and (i) OMS-PDMS with 1 wt% OMS_950 before and after contact.

increased to − 0.75 V due to the generation of negative tribo-charges, while that of the OMS-PDMS increased to − 1.46 V because of the additional charges stored by OMS. The decrease in the output when the OMS concentration exceeds 1 wt% can be attributed to the decrease in the effective electrification area of PDMS because OMS nanoparticles tended to appear on the surface, as can be seen from Fig. S2 [36]. As a result, the competition between the increase in charge storage sites and decrease in the effective PDMS area at high OMS concentrations led to the final decrease in the output of the TENG. To further prove that, an additional thin PDMS layer was added onto the surface of OMS-PDMS (2 wt%) to check if the output can be further increased since the influence of OMS nanoparticles on the effective PDMS area could be eliminated by this pure PDMS layer. As shown in Fig. S5, the V_{OC}, I_{SC} and Q_{SC} increased to 207 V, 15.7 μA and 81 nC, respectively, which are larger than those of 1 wt%, revealing the charge storage ability of OMS and importance of effective PDMS contact area. In addition, the stretchability of OMS-PDMS was also investigated, and the results are shown in Fig. S6, which reveal that the influence of adding OMS nanoparticles on the stretchability and tensile strength is negligible when the concentration of OMS is less than 1 wt%.

In addition to the concentration, the specific surface area (SSA) of OMS nanoparticles can also affect the output enhancement of the TENG since more charges are expected to be captured and stored with a larger SSA. To study the influence of the SSA on the output enhancement of the TENG, OMS nanoparticles of three different sizes were synthesized. Fig. 3a-c shows the SEM images of the three kinds of OMS nanoparticles with average lengths of 700 nm (OMS_700), 950 nm (OMS_950), and 1500 nm (OMS_1500). As seen from the TEM images of the side view in

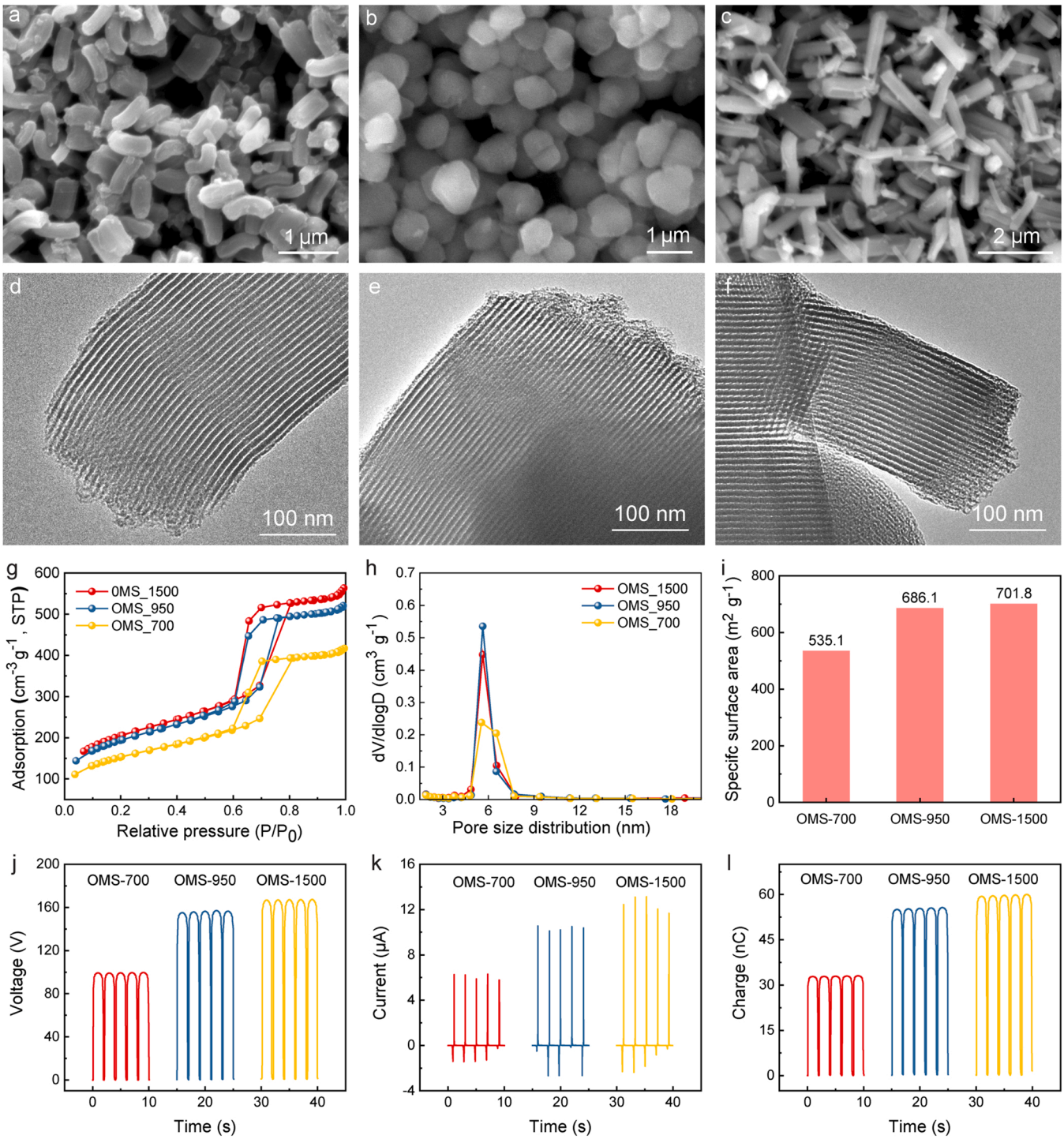

Fig. 3. SEM images of OMS_700 (a), OMS_950 (b) and OMS_1500 (c). TEM image of the lateral surface of OMS_700 (d), OMS_950 (e) and OMS_1500 (f). (g) Nitrogen adsorption-desorption isotherms of three kinds of OMS nanoparticles. (h) Pore size distributions of three kinds of OMS nanoparticles. (i) Specific surface areas of the OMS nanoparticles with different sizes. V_{OC} (j), I_{SC} (k) and Q_{SC} (l) of the TENG with different sizes of OMS nanoparticles (1 wt%).

Fig. 3d-f, all OMS nanoparticles possess regular parallel pore channels. Fig. 3g shows the nitrogen adsorption-desorption isotherms of the three kinds of OMS nanoparticles. H1-type hysteresis loops at relative pressures of approximately 0.6–0.7 can be clearly observed for the three OMS nanoparticles, confirming the existence of typical mesoporous structures and cylindrical channels. Calculated from the desorption branch, the pore size distributions can be obtained (Fig. 3h), centering at 5.63 nm, 5.63 nm, and 5.55 nm for OMS_1500, OMS_950, and OMS_700, respectively. The SSAs of the three kinds of OMS nanoparticles are summarized in Fig. 3i, among which OMS_1500 possesses the highest SSA.

The output performance of the TENG with OMS nanoparticles of different sizes is shown in Fig. 3j-l. Note that the concentration of the OMS nanoparticles in the OMS_PDMS hereafter is kept the same at 1 wt %. It is clearly observed that all three sizes of OMS nanoparticles have an obvious enhancement effect on the output performance of the TENG. With OMS_700 nanoparticles, which have the smallest SSA among the three sizes, the V_{OC}, I_{SC} and Q_{SC} of the TENG were 99 V, 6.3 μA and

33 nC, respectively, which already showed an enhancement of 94 %, 80 % and 57% compared with those of the TENG with pure PDMS. When the size and SSA of the OMS nanoparticles further increased, the output of the TENG also showed a corresponding increase. With the OMS_1500 nanoparticles featuring the largest SSA, the V_{OC}, I_{SC} and Q_{SC} of the TENG increased to 167.2 V, 13.1 μA and 60 nC, respectively, which were 228 %, 274 % and 186 %, respectively, of the outputs of the TENG with pure PDMS. It was interpreted that larger OMS nanoparticles with a larger SSA could provide more space to capture and store charges. As a result, the TENG with the OMS_1500 nanoparticle demonstrated the highest output performance for its largest SSA. To better understand the relationship between the SSA and the output enhancement, the SSAs of OMS nanoparticles of the three sizes and the Q_{SC} of the TENGs based on them were normalized by setting the SSA and Q_{SC} of the OMS_700 as 100 %. As Fig. S7 shows, the normalized Q_{SC} almost linearly increased with the increase in the normalized specific surface area.

The regular channels in OMS nanoparticles enable a large SSA to maximize the effective interface between PDMS and OMS, allowing more electrons transfer from PDMS to OMS. To prove that, a sample with the weight ratio of OMS_1500 to PDMS as 5:1 was prepared and a series of characterizations were conducted. Fig. 4a and b show the TEM micrographs of pure OMS_1500 and OMS_1500 mixed with a little amount of PDMS, which reveal that the clear channels of OMS nanoparticles became blurred, most likely due to the penetration of PDMS molecules into the channels. Moreover, the XRD pattern of OMS_1500 after mixing with PDMS showed that the 100 peak shifted to a larger 2θ (2θ=1.015°) compared with that of the pure OMS_1500 (2θ=0.929), indicating a smaller channel size (Fig. 4c). The decreased channel size was further proved by nitrogen adsorption-desorption measurements, as shown in Fig. 4d. After adding PDMS, the adsorption capacity and relative pressures both significantly decreased, because the channel size decreased from 6.52 to 3.69 nm (Fig. 4e). As a result, the pore volume and SSA of OMS nanoparticles showed a significant decrease, decreasing from 0.85 to 0.44 $cm^3\ g^{-1}$ and 716.6 to 278.6 $m^2\ g^{-1}$, respectively, as seen in Fig. 4f.

Hereafter, the OMS_1500 is used for further electrical characterizations and device fabrication for its highest output performance. The optimal concentration of OMS_1500 was firstly checked and the results are shown in Fig. S8. First, the output performance of the TENG under different working loads and frequencies was studied since the TENG is expected to work in a practical environment where the intensity and frequency of the ambient stimuli, such as vibration, are usually random. Fig. 5a-c shows the V_{OC}, I_{SC} and Q_{SC} of the TENG under different working loads (5, 10, 20, 30 and 40 N). When the load was 5 N, the V_{OC}, I_{SC} and Q_{SC} of the TENG were 93 V, 3.6 μA and 38 nC, respectively, which are even higher than those of the TENG with pure PDMS under 20 N. When the load increased from 5 N to 20 N, the output of the TENG had a relatively sharp increase due to the obvious increase in the effective contact area by increasing the load. Hereafter, the maximum effective contact area almost saturated at 20 N, so when the load further increased to 40 N, only a slight increase was observed in the output of the TENG. Specifically, the V_{OC}, I_{SC} and Q_{SC} of the TENG under 40 N were 177 V, 14.5 μA and 67 nC, respectively. The output performance of the TENG under different working frequencies is shown in Fig. 5d-f. V_{OC} and Q_{SC} remained constant, while I_{SC} increased linearly with increasing working frequency. This is because under a certain load, the effective contact area remains stable regardless of the working frequency, but the charge transfer rate between the two electrodes increases linearly with increasing frequency.

To further determine the cause behind the output enhancement, the accumulation of the V_{OC} of the TENG from the beginning of contact-separation to the stable state and the decay of V_{OC} from the stable state after stopping contact-separation were investigated. Fig. 6a shows the dynamic voltage accumulation of the TENGs as a function of time. The initial V_{OC} of the TENG with pure PDMS was 14 V, while that of the TENG with OMS-PDMS was 55 V. Such a high initial output of the OMS-PDMS can be attributed to the increased surface roughness after blending OMS nanoparticles. The triboelectric charges on the surface of the PDMS and Cu layers will start to accumulate with reciprocating contact separation and finally reach the saturation state. In the early

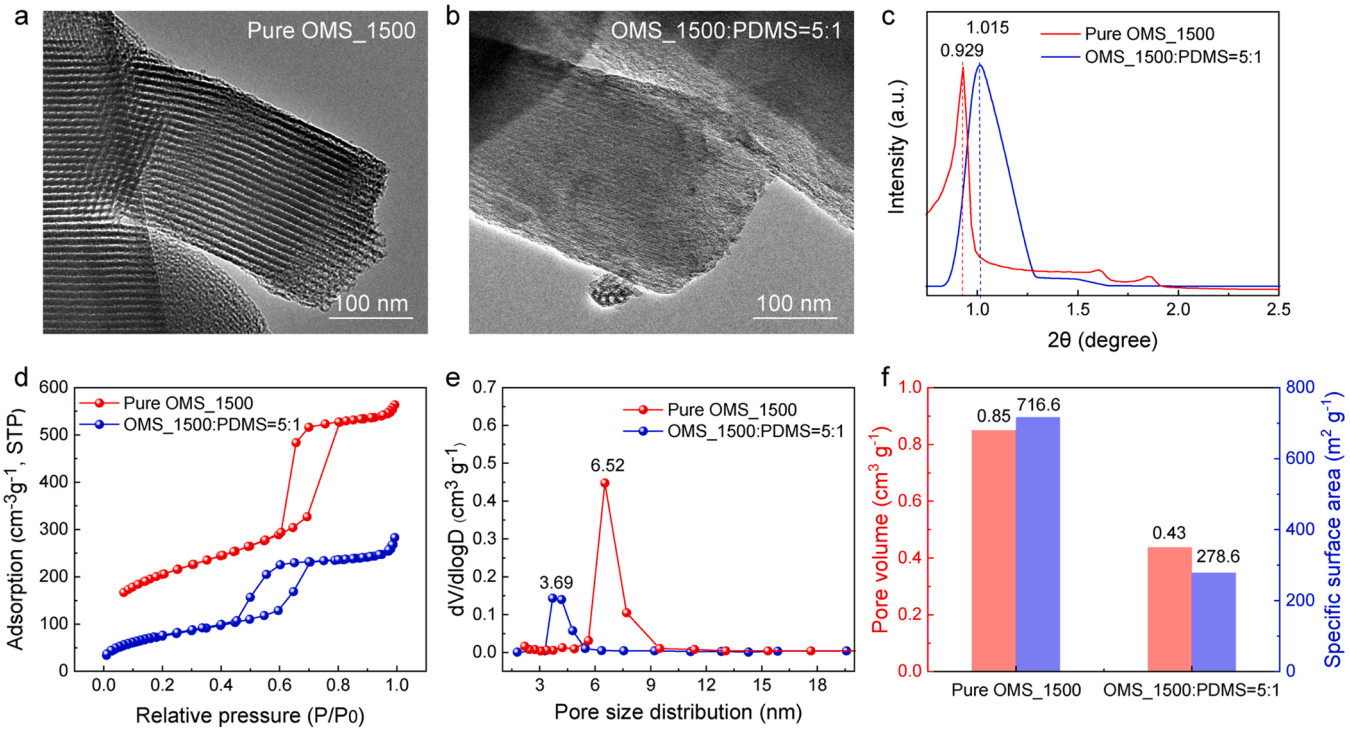

Fig. 4. TEM micrograph of (a) pure OMS_1500 and (b) OMS_1500 with 16.7 wt% of PDMS. (c) XRD patterns of pure OMS_1500 and OMS_1500 with 16.7 wt% of PDMS. (d) Nitrogen adsorption-desorption isotherms of pure OMS_1500 and OMS_1500 with 16.7 wt% of PDMS. (e) Pore size distributions of pure OMS_1500 and OMS_1500 with 16.7 wt% of PDMS. (f) Pore volumes and SSAs of pure OMS_1500 and OMS_1500 with 16.7 wt% of PDMS.

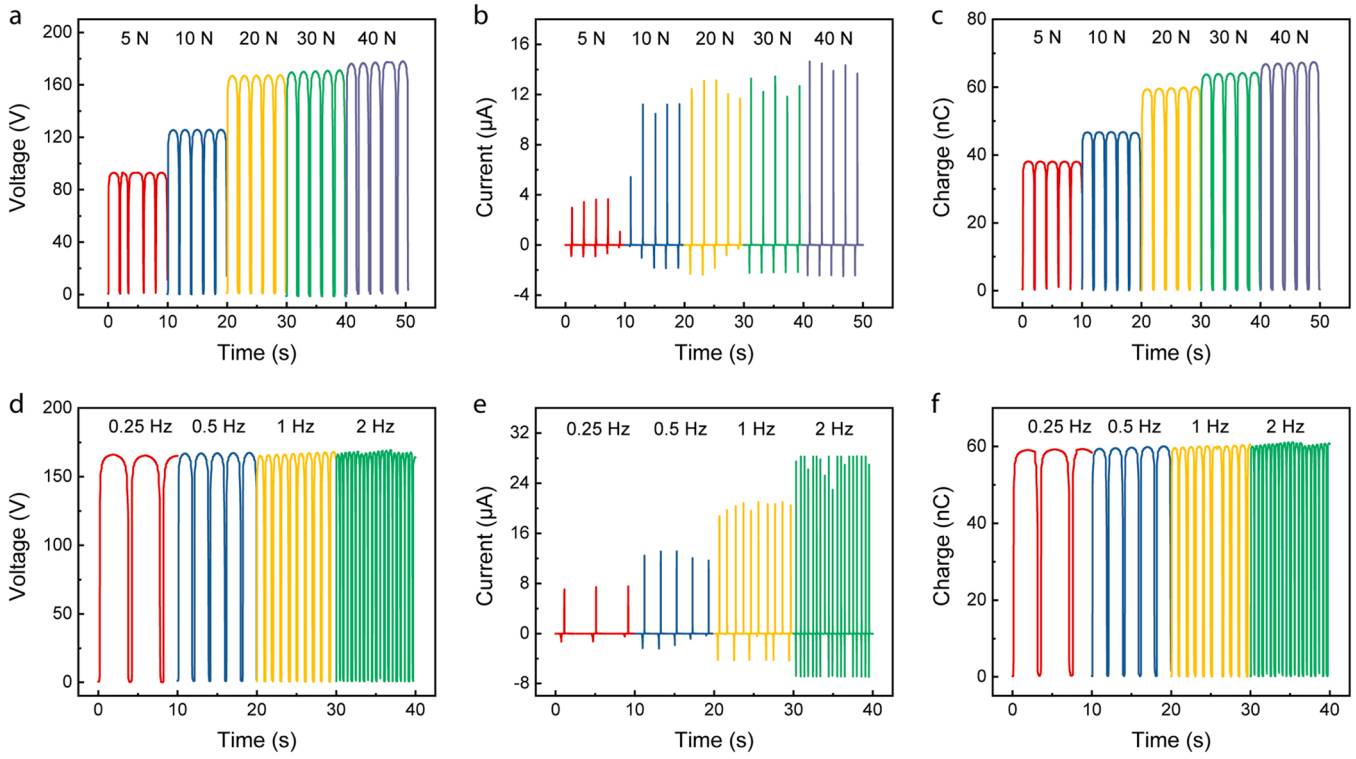

Fig. 5. V_{OC} (a), I_{SC} (b) and Q_{SC} (c) of the TENG with OMS_1500 under different working loads. V_{OC} (d), I_{SC} (e) and Q_{SC} (f) of the TENG with OMS_1500 under different working frequencies.

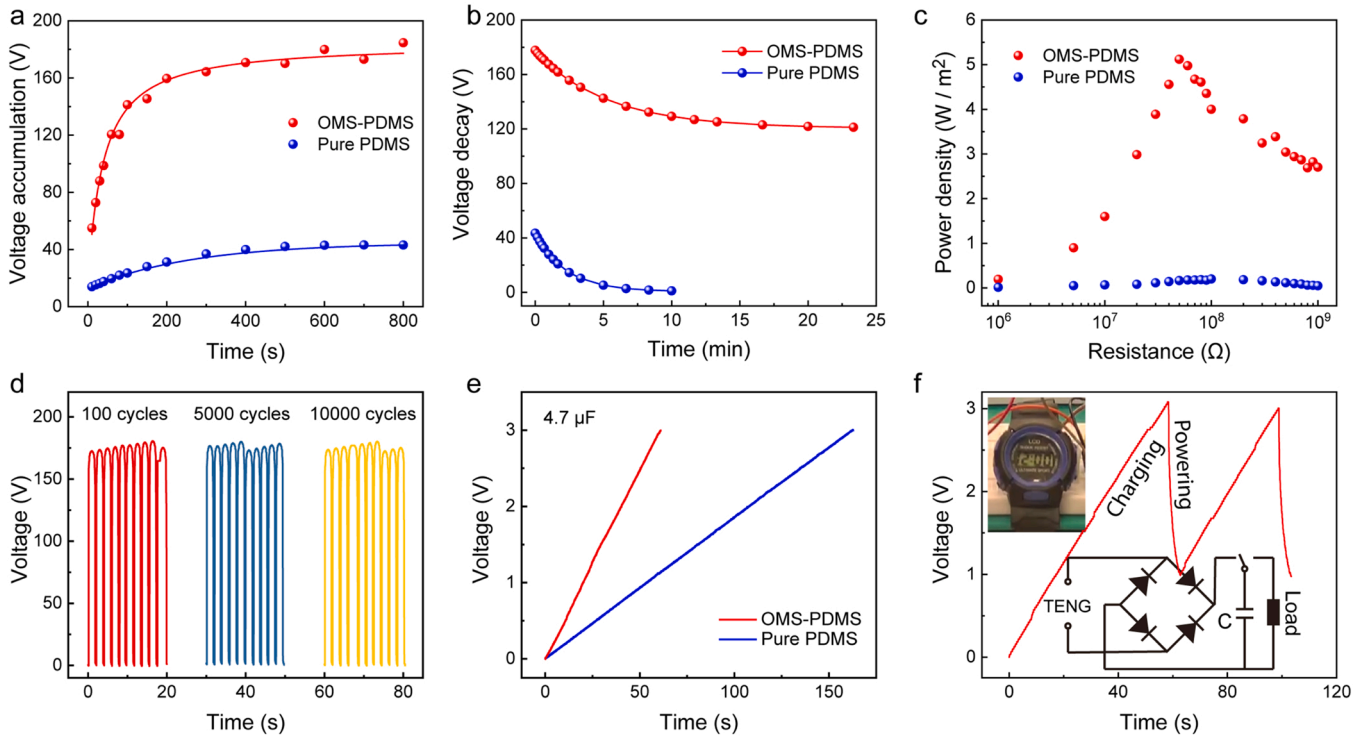

Fig. 6. (a) Voltage accumulation curves of the TENG with OMS-PDMS and pure PDMS. (b) Voltage decay curves of the TENG with OMS-PDMS and pure PDMS. (c) Instantaneous output power density of the TENG with OMS-PDMS and pure PDMS. (d) Long-term stability of the TENG with OMS-PDMS. (e) Charging a 4.7 μF capacitor by the TENG. (f) Powering an electronic watch by the TENG.

stage (0 ~ 100 s), the TENG with OMS-PDMS has a much faster increase rate (0.89 V/s) than the one with pure PDMS (0.11 V/s), which means a 7-fold enhancement in the increase rate. This is because in the early stage, surface charges can quickly penetrate into the interior of the PDMS due to the large concentration gradient and then be captured by the OMS nanoparticles. Afterwards, the V_{OC} of the TENG with pure

PDMS increased slowly and reached its maximum (43 V) after 500 s. Because of the large SSA of the OMS nanoparticles, the TENG with OMS-PDMS still showed an obvious increase in the $V_{OC,}$ and finally, its maximum value reached approximately 184 V. After the V_{OC} increased to the maximum and stabilized, the contact-separation movement between the two triboelectric layers was intentionally halted to observe the dynamic decay of voltage over time. As shown in Fig. 6b, the V_{OC} of the TENG with pure PDMS decreases quickly from the maximum to near zero, which indicates that the generated surface charges can quickly dissipate. However, with the OMS-PDMS, the V_{OC} of the TENG only decreased to 121 V after a long time, that is, 66 % of charges can be stored in the interior of the OMS-PDMS. These results clearly showed that the total charge accumulation and retention ability were largely enhanced by the introduction of OMS nanoparticles. The complete voltage-time curves of accumulation and decay of the TENGs with pure PDMS and OMS-PDMS are demonstrated in Fig. S9. Moreover, the charge storage of OMS nanoparticles was also verified by measuring the surface potential decay of the OMS-PDMS and pure PDMS after contact electrification with KPFM (Fig. S10). After contact, the surface potential of OMS-PDMS increased to − 1.46 V, while that of pure PDMS was only − 0.75 V. In the case of pure PDMS, the surface potential gradually decreased to near the initial value before contact. On the contrary, the OMS-PDMS showed a slower decay and finally the surface potential was stabilized at − 0.95 V, which is doubled than its initial value before contact. The reason is that the surface charges generated by contact electrification began to dissipate over time, while the body charges could stay for a long time. With extensive charges trapped by OMS nanoparticles inside PDMS, the TENG is expected to feature an improved performance stability on environmental parameters, such as temperature and humidity. As seen from Fig. S11a and b, with the temperature increased from 20 ℃ to 50 ℃, the V_{OC} of the TENGs showed a slight increase, and then decreased with further increasing temperature. Fig. S11d and e show that the V_{OC} of TENGs decreased with the increase of relative humidity. The outputs under different temperatures and relative humidities are normalized by setting the value at 20 ℃ and 30 % as 100 % (Fig. S11c and f), from which one can see that the TENG with OMS-TENG clearly showed a much improved performance stability over the fluctuation of environmental parameters due to the body trapped charges.

The instantaneous output power density of the TENGs with/without OMS nanoparticles was also calculated through impedance matching. The output voltage and current of the TENGs (20 N, 0.5 Hz) under different external resistors are shown in Fig. S12. The output voltage first increased with increasing external resistance and then saturated, while the current demonstrated a reverse trend, that is, first remained stable and then decreased. Therefore, the instantaneous output power density was subsequently calculated, as shown in Fig. 6c. The TENG with OMS-PDMS has a maximum instantaneous output power density of 5.26 W/m^2, which is approximately 26 times that of the TENG with pure PDMS (0.2 W/m^2). The enhanced output performance originating from the OMS nanoparticles also showed excellent stability over a long-term test (10,000 cycles), as shown in Fig. 6d. With the enhanced stable output, a 4.7 μF capacitor was charged to 3 V in 60 s by the TENG with OMS-PDMS, while it took 162 s for the TENG with pure PDMS to charge to the same voltage (Fig. 6e). To demonstrate the potential of the TENG with enhanced output performance as a power source in practical applications, an electronic watch was shown to be successfully powered by the TENG (20 N, 1 Hz), as shown in Fig. 6f and Video S1. Finally, compared to other high-SSA materials, such as 2D MXene and graphene applied in TENGs, OMS nanoparticles feature the advantages of high enhancement effect, high material yield and negligible influence on the transparency and strentchability of polymers, as can be seen from Table S1.

Supplementary material related to this article can be found online at doi:10.1016/j.nanoen.2023.108539.

3. Conclusion

In conclusion, we proposed ordered mesoporous SiO_2 nanoparticles with a large SSA as effective body charge storage sites to enhance the output performance of TENGs. The transferred charge of the TNEG sharply increased from 21 nC to 60 nC at the optimal OMS nanoparticle concentration of 1 wt%. A too high concentration of OMS nanoparticles could result in a decrease in the enhancement effect due to the reduced effective area of PDMS since OMS nanoparticles appeared on the surface of the composite. The enhancement effect of the OMS nanoparticles on the output performance of the TENG increased linearly with its SSA. In addition, compared with the TENG with pure PDMS, the TENG with OMS-PDMS demonstrated a superior charge retention ability. After stopping the contact-separation motion, the V_{OC} of the TENG with OMS-PDMS was retained at 68 % over a long time, while that of the pure PDMS quickly dropped to near 0 V. Finally, the instantaneous output power density of the TENG with OMS-PDMS was 26 times that of the TENG with pure PDMS, reaching 5.26 W/m^2. This work proposed OMS nanoparticles with a large specific surface area as effective charge storage sites to enhance the output performance of TENGs.

4. Experimental section

4.1. Synthesis of OMS nanoparticles

OMS nanoparticles were synthesized according to the previously reported soft-template method with some modifications [35,37]. Preparation of OMS_1500 and OMS_950: Pluronic P123 (1.8 g, $EO_{20}PO_{70}EO_{20}$, Mw = 5800) and glycerol (1.8 g) were added to 69 g aqueous acidic solution with different HCl concentrations (M_{HCl} = 1.0 M for OMS_1500, 1.5 M for OMS_950), followed by 6–10 h of stirring at 35 °C until all solutes were dissolved. Then, 3.87 g tetraethyl orthosilicate (TEOS, 99.9 %) was added to the above mixture under vigorous stirring at the same temperature. After 5 min of stirring, the mixture was aged at 35 °C for 24 h, followed by hydrothermal treatment at 100 °C for another 24 h. The sediment was collected by centrifugation, washed with deionized water, and dried at 80 °C overnight. Finally, OMS nanoparticles were obtained by calcining the above power at 550 °C for 5 h under an air atmosphere. The procedure for synthesizing OMS_700 is similar to that of OMS_1500, except the HCl concentration was increased to 2.5 M, and the amounts of other reactants were halved (0.9 g P123, 0.9 g glycerol, and 1.935 g TEOS).

4.2. Fabrication of the TENG

For the TENG with pure PDMS, PDMS (Sylgard 184 silicon elastomer) base and curing agent were mixed in a weight ratio of 10:1 followed by degassing in a vacuum chamber until the bubbles disappeared. Thereafter, the uncured PDMS was spin coated on the Cu-coated acrylic substrate, after which the curing process was conducted in an oven at 80 ℃ for 2 h. A Cu electrode deposited on another acrylic substrate was applied as another triboelectric layer paired with pure PDMS. For the TENG with OMS-PDMS, OMS nanoparticles were first ultrasonically dispersed in 10 ml hexane solvent in a 20 ml glass bottle. Then, 2 g of PDMS (Sylgard 184 silicon elastomer) base was added into the above mixture. Hereafter, the mixture was magnetically stirred with the bottle uncapped to allow the hexane to evaporate completely. After the evaporation of hexane, 0.2 g of PDMS curing agent was added into the mixture and magnetically stirred for 10 mins. Thereafter, the uncured OMS-PDMS mixture was spin coated on the Cu-coated acrylic substrate, followed by 2 hrs of curing at 80 ℃. A Cu electrode deposited on another acrylic substrate was applied as another triboelectric layer paired with pure PDMS. The two acrylic sheets were packed by a Kapton film (200 μm) using double-sided tape to form a contact-separation TENG, in which the copper layer faced the PDMS layer with a gap of 5 mm. The flexibility, light weight, and high elasticity modulus of the Kapton film

enables it to serve as a spring, ensuring the contact and separation of the two triboelectric layers.

4.3. Characterizations

Small-angle X-ray diffraction (XRD) patterns were collected by a D8 Advance diffractometer with a Cu Kα source (λ = 1.54 Å) operated at 40 kV and 40 mA. The porous features of the OMSs were measured using a porosimetry system (ASAP 2420, Micromeritics) at − 196 ℃. Before measurements, the samples were degassed at 300 ℃ for 10 h. Scanning electron microscopy (SEM) was performed on Lyra, Tescan. Transmission electron microscopy (TEM) was performed on a JEOL JEM-2020 operated at 200 kV. The surface roughness of the OMS-PDMS was investigated on a 3D surface profilometer (ContourX-200) and an object lens with a magnification of 50×. The water contact angles of the OMS-PDMS coatings were measured using an optical contact angle measurement instrument (Dataphysics 15EC). The electrical output of the TENG was measured using a Keithley electrometer (model 6514). The contact-separation process of the TENG was controlled with a contact-separation distance of 5 mm by a universal testing machine (MTS 810 system) with adjustable applied force and frequency.

Declaration of Competing Interest

The authors declare that they have no known competing financial interests or personal relationships that could have appeared to influence the work reported in this paper.

Data availability

Data will be made available on request.

Acknowledgments

W. L. acknowledges the China Scholarship Council, P. R. China for his Ph.D. scholarship (CSC, No. 201904910781).

CRediT authorship contribution statement

Wenjian Li: Conceptualization, Methodology, Investigation, Data curation, Formal analysis, Visualization, Validation, Writing – original draft. **Yinyu Xiang:** Methodology. **Wei Zhang:** Methodology. **Katja Loos:** Supervision, Writing – review & editing. **Yutao Pei:** Funding acquisition, Conceptualization, Supervision, Writing – review & editing.

Appendix A. Supporting information

Supplementary data associated with this article can be found in the online version at doi:10.1016/j.nanoen.2023.108539.

References

[1] Z.L. Wang, Triboelectric nanogenerator (TENG) – sparking an energy and sensor revolution, Adv. Energy Mater. 10 (2020), 2000137.
[2] Y. Wang, Y. Yang, Z.L. Wang, Triboelectric nanogenerators as flexible power sources, npj Flex. Electron 1 (2017) 10.
[3] J. Luo, Z.L. Wang, Recent progress of triboelectric nanogenerators: From fundamental theory to practical applications, EcoMat 2 (2020), e12059.
[4] W. Li, Y. Liu, S. Wang, W. Li, G. Liu, J. Zhao, X. Zhang, C. Zhang, Vibrational triboelectric nanogenerator-based multinode self-powered sensor network for machine fault detection, IEEE/ASME Trans. Mechatron. 25 (2020) 2188–2196.
[5] W. Li, L. Lu, X. Fu, C. Zhang, K. Loos, Y. Pei, Karman vortex street driven membrane triboelectric nanogenerator for enhanced ultra-low speed wind energy harvesting and active gas flow sensing, ACS Appl. Mater. Interfaces 14 (2022) 51018–51028.
[6] Y. Zou, V. Raveendran, J. Chen, Wearable triboelectric nanogenerators for biomechanical energy harvesting, Nano Energy 77 (2020), 105303.
[7] F. Xi, Y. Pang, G. Liu, S. Wang, W. Li, C. Zhang, Z.L. Wang, Self-powered intelligent buoy system by water wave energy for sustainable and autonomous wireless sensing and data transmission, Nano Energy 61 (2019) 1–9.
[8] W. Li, L. Lu, A.G.P. Kottapalli, Y. Pei, Bioinspired sweat-resistant wearable triboelectric nanogenerator for movement monitoring during exercise, Nano Energy 95 (2022), 107901.
[9] X. Lan, W. Li, C. Ye, L. Boetje, T. Pelras, F. Silvianti, Q. Chen, Y. Pei, K. Loos, Scalable and degradable dextrin-based elastomers for wearable touch sensing, ACS Appl. Mater. Interfaces 15 (2023) 4398–4407.
[10] H. Chen, C. Xing, Y. Li, J. Wang, Y. Xu, Triboelectric nanogenerators for a macro-scale blue energy harvesting and self-powered marine environmental monitoring system, Sustain. Energy Fuels 4 (2020) 1063–1077.
[11] X. Xiao, X. Zhang, S. Wang, H. Ouyang, P. Chen, L. Song, H. Yuan, Y. Ji, P. Wang, Z. Li, M. Xu, Z.L. Wang, Honeycomb structure inspired triboelectric nanogenerator for highly effective vibration energy harvesting and self-powered engine condition monitoring, Adv. Energy Mater. 9 (2019), 1902460.
[12] S. Li, D. Liu, Z. Zhao, L. Zhou, X. Yin, X. Li, Y. Gao, C. Zhang, Q. Zhang, J. Wang, Z. L. Wang, A. Fully, Self-powered vibration monitoring system driven by dual-mode triboelectric nanogenerators, ACS Nano 14 (2020) 2475–2482.
[13] D. Wan, J. Yang, X. Cui, N. Ma, Z. Wang, Y. Li, P. Li, Y. Zhang, Z.-H. Lin, S. Sang, H. Zhang, Human body-based self-powered wearable electronics for promoting wound healing driven by biomechanical motions, Nano Energy 89 (2021), 106465.
[14] R. Guo, Y. Fang, Z. Wang, A. Libanori, X. Xiao, D. Wan, X. Cui, S. Sang, W. Zhang, H. Zhang, J. Chen, Deep learning assisted body area triboelectric hydrogel sensor network for infant care, Adv. Funct. Mater. 32 (2022).
[15] C. Zhang, L. Zhou, P. Cheng, X. Yin, D. Liu, X. Li, H. Guo, Z.L. Wang, J. Wang, Surface charge density of triboelectric nanogenerators: theoretical boundary and optimization methodology, Appl. Mater. Today 18 (2020), 100496.
[16] D. Liu, L. Zhou, S. Cui, Y. Gao, S. Li, Z. Zhao, Z. Yi, H. Zou, Y. Fan, J. Wang, Z. L. Wang, Standardized measurement of dielectric materials' intrinsic triboelectric charge density through the suppression of air breakdown, Nat. Commun. 13 (2022) 6019.
[17] J. Huang, X. Fu, G. Liu, S. Xu, X. Li, C. Zhang, L. Jiang, Micro/nano-structures-enhanced triboelectric nanogenerators by femtosecond laser direct writing, Nano Energy 62 (2019) 638–644.
[18] Y. Yu, X. Wang, Chemical modification of polymer surfaces for advanced triboelectric nanogenerator development, Extrem. Mech. Lett. 9 (2016) 514–530.
[19] T. Zhou, L. Zhang, F. Xue, W. Tang, C. Zhang, Z.L. Wang, Multilayered electret films based triboelectric nanogenerator, Nano Res. 9 (2016) 1442–1451.
[20] X. Xie, X. Chen, C. Zhao, Y. Liu, X. Sun, C. Zhao, Z. Wen, Intermediate layer for enhanced triboelectric nanogenerator, Nano Energy 79 (2021), 105011.
[21] H. Jiang, H. Lei, Z. Wen, J. Shi, D. Bao, C. Chen, J. Jiang, Q. Guan, X. Sun, S.-T. Lee, Charge-trapping-blocking layer for enhanced triboelectric nanogenerators, Nano Energy 75 (2020), 105011.
[22] C. Wu, T.W. Kim, J.H. Park, H. An, J. Shao, X. Chen, Z.L. Wang, Enhanced triboelectric nanogenerators based on MoS(2) monolayer nanocomposites acting as electron-acceptor layers, ACS Nano 11 (2017) 8356–8363.
[23] Y. Guo, Y. Cao, Z. Chen, R. Li, W. Gong, W. Yang, Q. Zhang, H. Wang, Fluorinated metal-organic framework as bifunctional filler toward highly improving output performance of triboelectric nanogenerators, Nano Energy 70 (2020), 104517.
[24] Y. Liu, J. Ping, Y. Ying, Recent progress in 2D-nanomaterial-based triboelectric nanogenerators, Adv. Funct. Mater. 31 (2021), 2009994.
[25] X. Xia, J. Chen, G. Liu, M.S. Javed, X. Wang, C. Hu, Aligning graphene sheets in PDMS for improving output performance of triboelectric nanogenerator, Carbon 111 (2017) 569–576.
[26] M. Kim, S.H. Kim, M.U. Park, C. Lee, M. Kim, Y. Yi, K.-H. Yoo, MoS2 triboelectric nanogenerators based on depletion layers, Nano Energy 65 (2019), 104079.
[27] S. Liu, W. Zheng, B. Yang, X. Tao, Triboelectric charge density of porous and deformable fabrics made from polymer fibers, Nano Energy 53 (2018) 383–390.
[28] W. Li, Y. Pei, C. Zhang, A.G.P. Kottapalli, Bioinspired designs and biomimetic applications of triboelectric nanogenerators, Nano Energy 84 (2021), 104079.
[29] Q. Zheng, L. Fang, H. Guo, K. Yang, Z. Cai, M.A.B. Meador, S. Gong, Highly porous polymer aerogel film-based triboelectric nanogenerators, Adv. Funct. Mater. 28 (2018).
[30] J.-K. Kim, G.H. Han, S.-W. Kim, H.J. Kim, R. Purbia, D.-M. Lee, J.K. Kim, H. J. Hwang, H.-C. Song, D. Choi, S.-W. Kim, Z.L. Wang, J.M. Baik, Electric-field-driven interfacial trapping of drifting triboelectric charges via contact electrification, Energy Environ. Sci. 16 (2023) 598–609.
[31] P. Giinther, SiO2 electrets for electric-field generation in sensors and actuators, Sens. Actuators, A 32 (1992) 357–360.
[32] X. Ding, Y. Li, Y. Si, X. Yin, J. Yu, B. Ding, Electrospun polyvinylidene fluoride/SiO2 nanofibrous membranes with enhanced electret property for efficient air filtration, Compos. Commun. 13 (2019) 57–62.
[33] N. Yuan, J. Li, SiO2 film electret with high surface potential stability, Appl. Surf. Sci. 252 (2005) 455–460.
[34] Q. Wang, Z. Wang, T. Zheng, X. Zhou, W. Chen, D. Ma, Y. Yang, S. Huang, Size control of SBA-15 by tuning the stirring speed for the formation of CMK-3 with distinct adsorption performance, Nano Res. 9 (2016) 2294–2302.
[35] D.Y. Zhao, J.L. Feng, Q.S. Huo, N. Melosh, G.H. Fredrickson, B.F. Chmelka, G. D. Stucky, Triblock copolymer syntheses of mesoporous silica with periodic 50 to 300 angstrom pores, Science 279 (1998) 548–552.
[36] J. Chen, H. Guo, X. He, G. Liu, Y. Xi, H. Shi, C. Hu, Enhancing performance of triboelectric nanogenerator by filling high dielectric nanoparticles into sponge PDMS film, ACS Appl. Mater. Interfaces 8 (2016) 736–744.
[37] Y. Wang, F. Zhang, Y. Wang, J. Ren, C. Li, X. Liu, Y. Guo, Y. Guo, G. Lu, Synthesis of length controllable mesoporous SBA-15 rods, Mater. Chem. Phys. 115 (2009) 649–655.